minerals

MDPI

Article

Audio Magnetotellurics Study of the Geoelectric Structure across the Zhugongtang Giant Lead–Zinc Deposit, NW Guizhou Province, China

Regean Pitiya [1], Mao Lu [2], Rujun Chen [1,*], Guanhai Nong [2], Siwen Chen [1], Hongchun Yao [1], Ruijie Shen [1] and Enhua Jiang [1]

[1] Hunan Key Laboratory of Nonferrous Resources and Geological Hazards Exploration, Key Laboratory of Metallogenic Prediction of Nonferrous Metals, Ministry of Education, Innovation and Entrepreneurship Education Center for AIoT, Geology and Geophysics, School of Geosciences and Info-Physics, Central South University, Changsha 410083, China
[2] Non-Ferrous Metals and Nuclear Industry Geological Exploration Bureau of Guizhou, Guiyang 541004, China
* Correspondence: chrujun12358@gmail.com

Abstract: Non-invasive geophysical exploration methods a play key role in the exploration of ore deposits. In the present study, the audio-frequency magnetotelluric (AMT) method was applied to metallic mineral exploration. The metallic mineral deposit targeted was the recently discovered super large lead–zinc deposit of the Zhugongtang mining area of Hezhang County in the northwestern Guizhou province in China. The main objectives of this study were to estimate the geoelectric strike and generate geoelectric models that estimate both the depth and distribution of resistivity structures across the deposit. To achieve the objectives, we deployed sixty-one (61) AMT survey sites with an interstation separation of 20 m on a 1280 m survey track perpendicular to the geological strike across the Zhugongtang deposit. We operated in fifty-three (53) frequencies in the range 1–10,400 Hz to record the resistivity distribution of subsurface to a depth of more than 1200 m. The results from the AMT data computations estimated the geoelectric strike that varies between NE285° and NE315°. This range of strikes suggested that structures across the deposit are oriented in the NW–SE direction. Obtained two-dimensional (2D) models elucidated a remarkably low resistivity body (<15 Ωm) at an elevation of less than 1600 m above sea level (>0.50 km depth), thus extending to great depth and were interpreted as lead–zinc mineralization. Furthermore, low resistivity (<63 Ωm) features were imaged both in superficial and deeper depths and interpreted as shale, sandstone, claystone, and silty mudstone units. Dolomite and limestone lithologies were found widely distributed with high resistivity (>1000 Ωm). Bioclastic limestone and dolomite limestone were inferred and characterized by moderate-high resistivity (>250 Ωm) and were not widely distributed. A unit of basalts was found with moderate resistivity (>63 Ωm). In addition, it was also found that regions with high number of faults tend to have low resistivity values compared to regions with a low fault number. In summary, this case study presents the results of applying an AMT approach to explore the conductivity characteristics of structures across the Zhugongtang deposit. The findings may contribute to the literature about this deposit.

Keywords: Zhugongtang deposit; lead–zinc; Sichuan-Yunnan-Guizhou Metallogenic Province (SYGMP); audio magnetotelluric; inversion

Citation: Pitiya, R.; Lu, M.; Chen, R.; Nong, G.; Chen, S.; Yao, H.; Shen, R.; Jiang, E. Audio Magnetotellurics Study of the Geoelectric Structure across the Zhugongtang Giant Lead–Zinc Deposit, NW Guizhou Province, China. *Minerals* **2022**, *12*, 1552. https://doi.org/10.3390/min12121552

Academic Editor: Paul Alexandre

Received: 11 October 2022
Accepted: 28 November 2022
Published: 30 November 2022

1. Introduction

In the modern era, mineral resources are being used at an unprecedented rate by humanity. Demand will continue to rise as a result of population growth, urbanization, and technological advancements such as the transition from fossil fuel dependency to green technology [1,2]. For many years, industries and academia have implemented mineral resource development to meet the demand for mineral resources. In mineral resource

development, exploration and characterization of mineralization have and continue to play key roles [3]. Furthermore, mineral studies and research projects have shifted from the conventional approach of recognition of surface mineralization (outcrop) as a preliminary indicator for a potential mineral resource [4], to the detection of deep-seated orebodies without surface manifestation [5,6]. In this approach, prospection methods such as geological, drilling, geochemical and geo-physical are used [7]. Among these prospection methods, the geophysical methods generally have the advantage of great detection depths and high resolution, which result in the provision of rich information for deep ore prospection [8]. Since the development of electromagnetic (EM) geophysical methods in the 1950s, the methods have been extensively applied to mapping lateral and vertical resistivity variation in the subsurface. For example, natural source audio magnetotelluric (AMT) and controlled source AMT (CSAMT) are widely applied to metallic mineral [9–15], groundwater [16–19], and geothermal system exploration [20–24], whereas the natural source broadband magnetotelluric (BBMT) method is widely used in the field of deep structure explorations, including lower crust and upper mantle structure [25–27], The radio magnetotelluric (RMT) method has been applied in engineering investigations to aid urban infrastructure planning [28–31]. The RMT method is also gaining applications in land characterization, for cases such as waste sites, landslides, etc. [32,33].

In this paper, we investigate the recently discovered Zhugongtang lead–zinc deposit in the northwestern (NW) Guizhou province of China with the AMT approach. This deposit is the largest lead–zinc mineralization in the province and is buried in deep subsurface without significant outcrops. This lead–zinc deposit has potential economic value. Therefore, the development and utilization of its resources are expected to alleviate local poverty and provide strong mineral resource support for the development of the Yangtze River economic belt. Since commercial mining of the deposit has not yet started, we attempt to examine the electrical resistivity structures across the deposit with the following objectives: (i) approximate geoelectric strike distribution, (ii) estimate deposit minimum burial depth, and (iii) generate two-dimensional (2D) geoelectric models that estimate the resistivity of structures across the deposit. The formulated objectives above form a guide to better understand the conductivity characteristics of the deposit we studied.

2. Geological Setting

The Zhugongtang deposit is a member of the lead–zinc deposits (such as Nayongzhi, Shaojiwan, Tianqiao, Huize, Tianboashan, Daliangzi, Fule, etc.) of the Sichuan-Yunnan-Guizhou Metallogenic Province (SYGMP) (Figure 1b). The SYGMP is a mineral-rich region hosting world-class deposits and spans an area of about 170,000 km^2 of the southwest Yangtze Block in the South China Block (Figure 1a) [34,35]. The South China Block is reported to have undergone multiple tectonic episodes, including the amalgamation and remobilization of Yangtze and Cathaysia block, with a strength of approximately 950–900 Ma [36,37], and the collision with North China and Indochina blocks to the north and south, respectively [35]. It is generally suggested that this series of tectonic events was vital for the mineralization of thrust-hosted epigenetic zinc–lead (Zn–Pb) deposits in the region [38,39]. These thrust-hosted epigenetic Zn–Pb deposits in SYGMP generally have very high ore grades of Zn–Pb at >10%, with a maximum of 30–35% [40]. The ore-forming fluids of these deposits have been reported to have characteristic low temperatures of 120–280 °C. They exhibit spatial and genetic association with igneous activities of the Emeishan large igneous province (ELIP) [41]. The SYGMP region has the highest concentration of epigenetic hydrothermal Pb–Zn polymetallic deposits hosted in the Neoproterozoic to early Permian carbonate strata in thrust and fold systems [42]. About 17% of the known global lead and zinc resources are hosted in this region and more than 440 deposits and mineral occurrences have been reported [40,43,44]. The SYGMP is bounded by three regional fault belts in the South West Yangtze Block: the NW-trending Kangding–Yiliang–Shuicheng fault (KYSF), the NS-trending Anninghe–Lvzhijiang fault (ALF), and the NE trending Mile–Shizong–Shuicheng fault (MSSF) (Figure 1a) [35,45]. These faults extend into the basement rocks

and were continually activated by the multiphase orogenic activities, including the Wuyi-Yunkai orogeny that occurred between the Middle Ordovician (>460 Ma) and the end of the Silurian (420–415 Ma) [46]. Indosinian orogeny, with an age estimate of 244 ± 7 Ma [47], and the Yanshanian orogeny that occurred during the Jurassic Period [48] in the South China Block. Regional stratigraphy includes a Mesoproterozoic folded meta-sandstone and slate basement overlain by Paleozoic to early Mesozoic submarine sedimentary sequences and Jurassic to Cenozoic terrigenous sedimentary sequences [35].

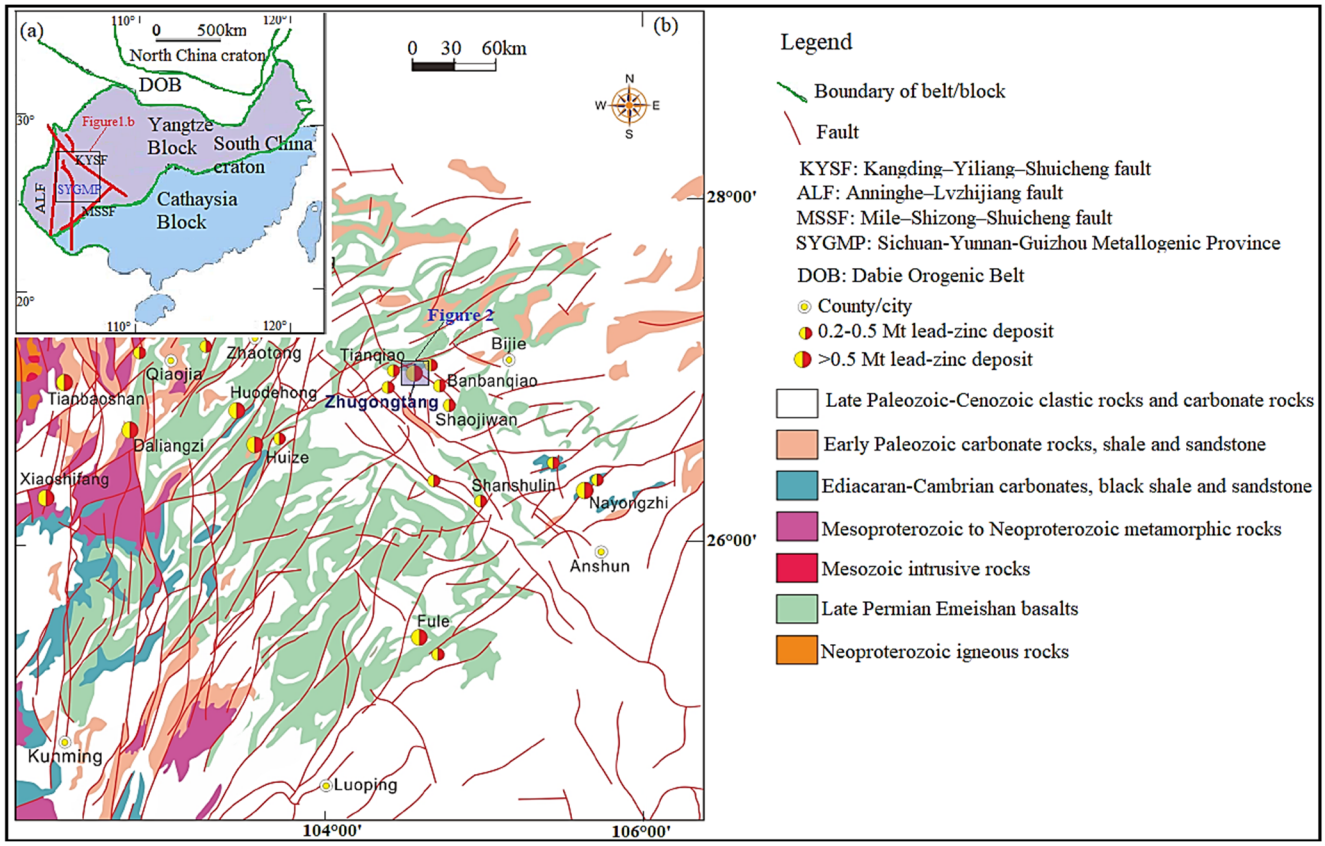

Figure 1. (**a**) Regional geological setting showing the location of the Sichuan–Yunnan–Guizhou Metallogenic Province (SYGMP) in South China; (**b**) geological sketch map of SYGMP showing regional structures, strata, and the distribution of lead–zinc deposits in the metallogenic province (modified from [35,45]).

3. Deposit Geology

The exposed rocks in the Zhugongtang orefield are predominantly sedimentary covers from the early Silurian to the late Permian periods (Figure 2) [49]. Early Silurian Hanjiadian Fm sandstone and silty mudstones are the oldest rocks in this region [35]. The Devonian Wangchengpo and Yaosuo Fms, which are made up of dolostone, siliceous dolostone, limestone, and dolomitic limestone, unconformably overlay the old rock formations [35]. The Carboniferous and Permian layers unconformably overlay the Devonian Yaosuo Fm [35]. The most prominent controlling structures include the NW and NE trending faults, as well as small interlayer fractures. Lead–zinc orebodies in this area occur as stratiform, lenticular, and steeply dipping veins inside the NW-trending F1 and F2 faults (Figures 2 and 3), as well as in the interlayer fracture zones [35,49]. The types of ore textures are mainly disseminated, massive, and vein. Ore minerals include sphalerite, galena, and pyrite. Gangue minerals include dolomite, calcite, and minor quartz and K feldspar [35].

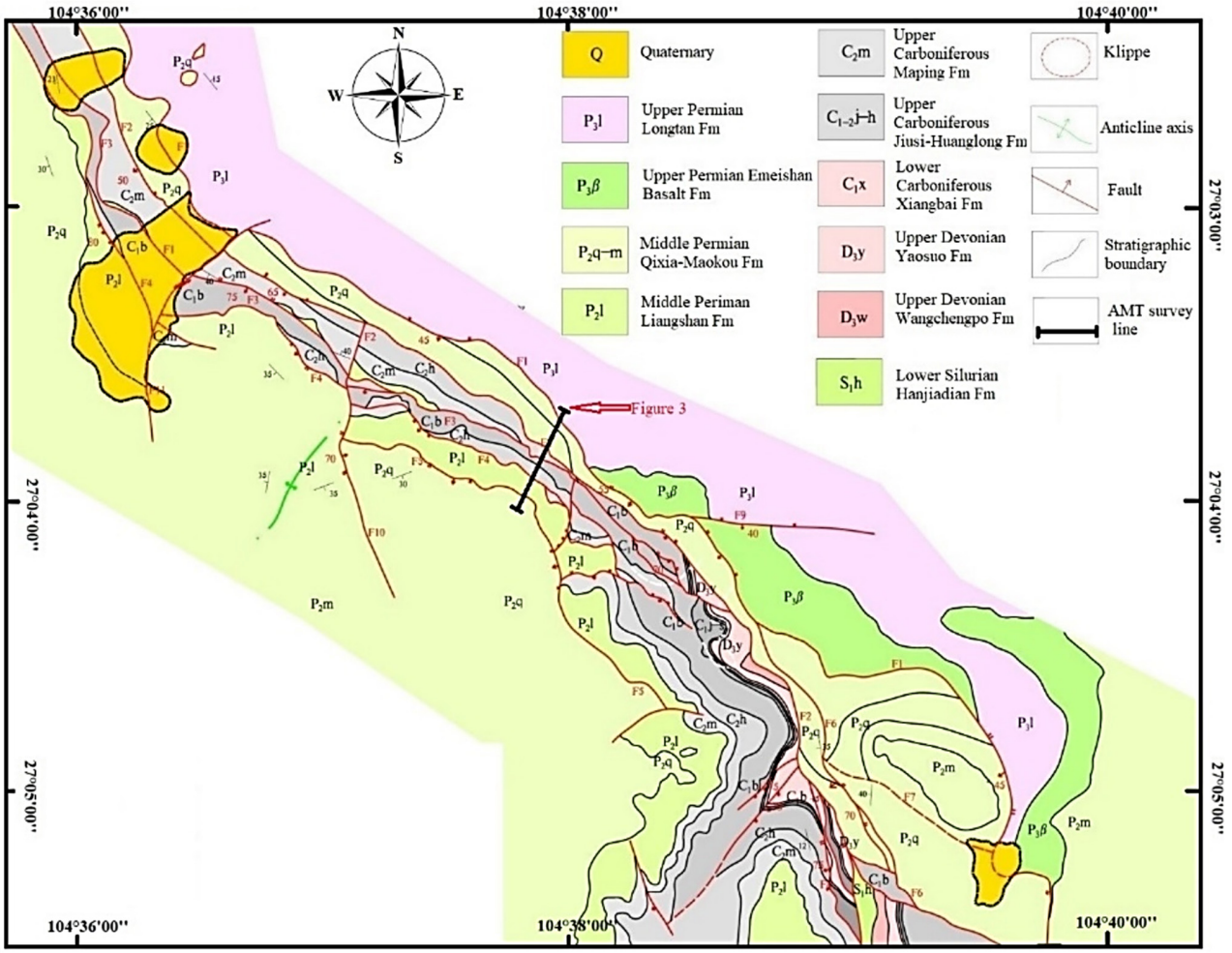

Figure 2. Geological map of Zhugongtang orefield with AMT survey line on top of an interpretation of the geology. Fm: Formation.

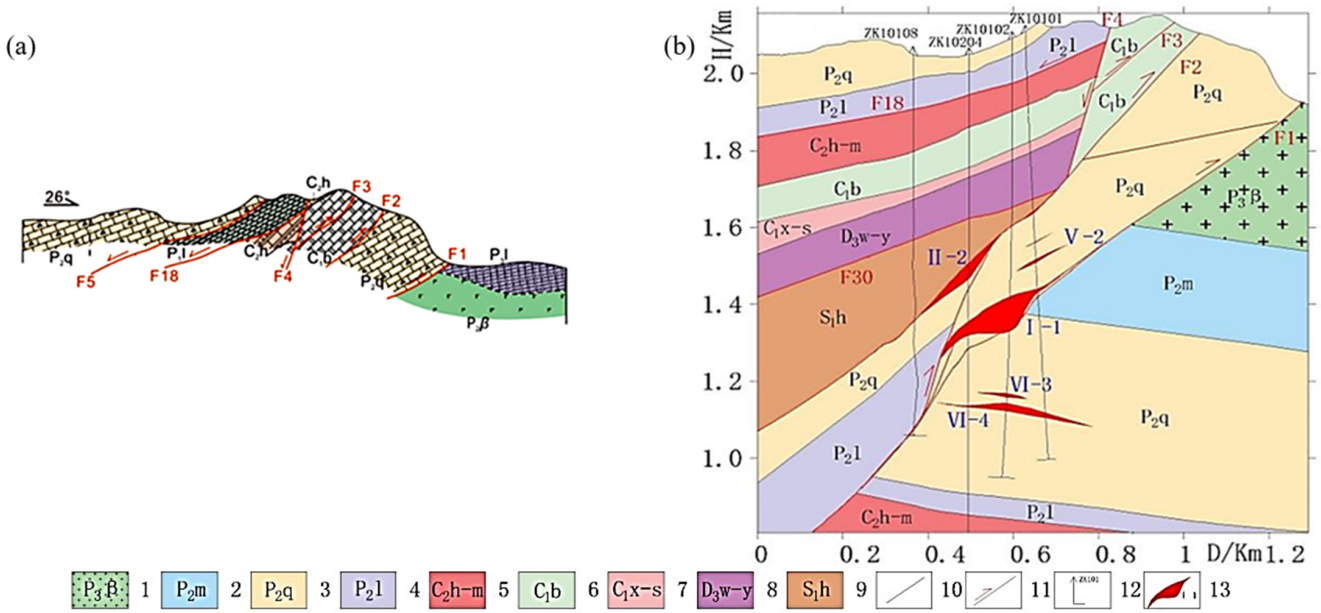

Figure 3. Geological cross-section of the Zhugongtang deposit on the AMT survey line: (**a**) showing

the thrust system (adopted from [35]), (**b**) stratigraphic boundary and boreholes (from after [35]). H: elevation, D: distance, 1: upper Permian Emeishan basalt formation; 2: middle Permian Maokou formation; 3: middle Permian Qixia formation; 4: middle Permian Liangshan formation; 5: upper Carboniferous Huanglong–Maping formation; 6: lower Carboniferous Baizuo formation; 7: lower Carboniferous Xiangbai formation; 8: upper Devonian Wangchengpo–Yaosuo formation; 9: lower Silurian Hanjiadian formation; 10: stratigraphic boundaries; 11: faults; 12: drill holes and numbers; 13: orebody number.

4. Methods

In this investigation, the magnetotelluric method is applied to mineral exploration. The magnetotelluric method was first introduced by Andrey Nikolayevich Tikhonov in 1950 [50] and Louis Cagniard in 1953 [51]. Later, the method was further developed by Cantwell Thomas in 1960 [52,53] and Keeva Vozoff [54]. The method probes the electrical structure of the subsurface using either the artificial (controlled) or natural electromagnetic (EM) field as the field source [55]. In artificial or controlled magnetotelluric, the EM signals are generated by EM transmitters. The radio magnetotelluric (RMT) method, which uses civilian and military radio transmitters broadcasting in the frequency range of 10 kHz to 1 MHz, is an example of artificial source magnetotellurics [56]. In natural magnetotelluric exploration, the electromagnetic fields originate from global lightning or sferics (short period signals) and solar wind activities in the ionosphere (long-period signals). Based on frequency, the natural magnetotelluric fields can be clustered into audiomagnetotellurics (AMT) with frequencies f = 1–10,000 Hz and broadband magnetotelluric (BBMT) with f = 0.001–300 Hz [57]. In principle, the earth is viewed as a horizontal medium and the magnetotelluric fields as the plane electromagnetic waves are projected vertically onto the ground (earth) [21]. When these waves impinge the ground, large proportions of them are reflected, and a small fraction is transmitted into the subsurface [54]. Electromagnetic induction (i.e., the fluctuating magnetic field) causes telluric currents to flow into the subsurface. The magnitude depends on electrical conductivity [58]. Diffusive signal transmission occurs, resulting in signal attenuation/decay as the depth increases. The skin depth (δ), which is the depth (in meters) of electromagnetic wave decay in the subsurface when the amplitude diminishes to 1/e of its value at the surface, is given by the following expression [59]:

$$\delta = \sqrt{\frac{\rho}{\pi f \mu}} \approx 500\sqrt{\frac{\rho}{f}} \quad (1)$$

where ρ is the resistivity (Ωm), f is the frequency (Hz), and μ is the magnetic permeability (H/m). The skin depth is controlled mainly by the conductivity (inverse of resistivity) of rocks and the operating frequency used. The most common sources for enhanced conductivity in the subsurface include graphite or carbon films, interconnected metallic minerals, aqueous fluid, partial melt, and any combination of these [60].

The above expression shows that the skin depth is inversely proportional to frequency. This implies that low frequencies penetrate to greater depths, and high frequencies are limited to shallow depths. On the ground, orthogonal electromagnetic field components are observed. The frequency response reflects the distribution of the electrical properties of the subsurface medium [61]. The variation of the magnetotelluric field component with time is converted into a frequency spectrum. Magnetotelluric frequency domain responses—such as apparent resistivity and the impedance phase—can be computed. Apparent resistivity is calculated using the following expression:

$$\rho = \frac{1}{5f}\left|\frac{E_x}{H_y}\right|^2 \quad (2)$$

where f is the frequency in Hz, ρ is the resistivity in Ωm, E_x is the electric field and H_y is the magnetic field.

5. Data Acquisition and Processing

In November 2021, we carried out an AMT survey comprising sixty-one (61) AMT stations distributed along a SW-NE striking profile across the Zhugongtang deposit (Figure 2). The length of the profile line was 1280 m, stretching perpendicular to the geological strike with an inter-AMT station separation of 20 m (Figure 2). Due to tough terrains (cliffs) in the north-east section of the profile, four (4) AMT sites were abandoned between the AMT-59 and AMT-60 sites. The AMT time-variant field or time series data were acquired using the GSEM-W10 system (developed by Giant Sequoia Artificial Intelligence Technology Co., Ltd., Changsha, China) (Figure 4) [62]. The AMT data were collected in fifty-three (53) frequencies in the range of 1 Hz to 10,400 Hz for thirty-five (35) minutes at each station by measuring two horizontal components of the electric field (Ex and Ey) and the two orthogonal components of the magnetic field (Hx and Hy). The X- and Y- directions were assigned along the profiles toward the north (N) and east (E), respectively. Data for magnetic field variations were obtained using induction coil magnetometers (ICM) and data for electric field variations were obtained by two pairs of non-polarizable lead–chloride electrodes (Pb–PbCl2). Prior to measurement, each electric field measurement point was soaked with water to reduce their contact resistivity. The condition of each station was recorded for sources of interference. Identified sources of interference included roads, high voltage power lines, and communication cables, many of which were observed in the middle of the survey lines. Utilizing the GSEM-pros software (that is provided with the acquisition unit) [63], the collected AMT time series field data were processed, transformed into frequency domain, and the cross-power spectra were computed. The cross-power spectra estimate the impendence tensor as a function of frequency. The impendence tensor contains information about the dimensionality and the strike of the subsurface structures. This is discussed in the next section. In general, the data quality was good at most sites, except for data collected at and near the interference (AMT23, Figure 5) sources mentioned above.

Figure 4. AMT field instruments used and the covers in the area. ICM: induction coil magnetometers.

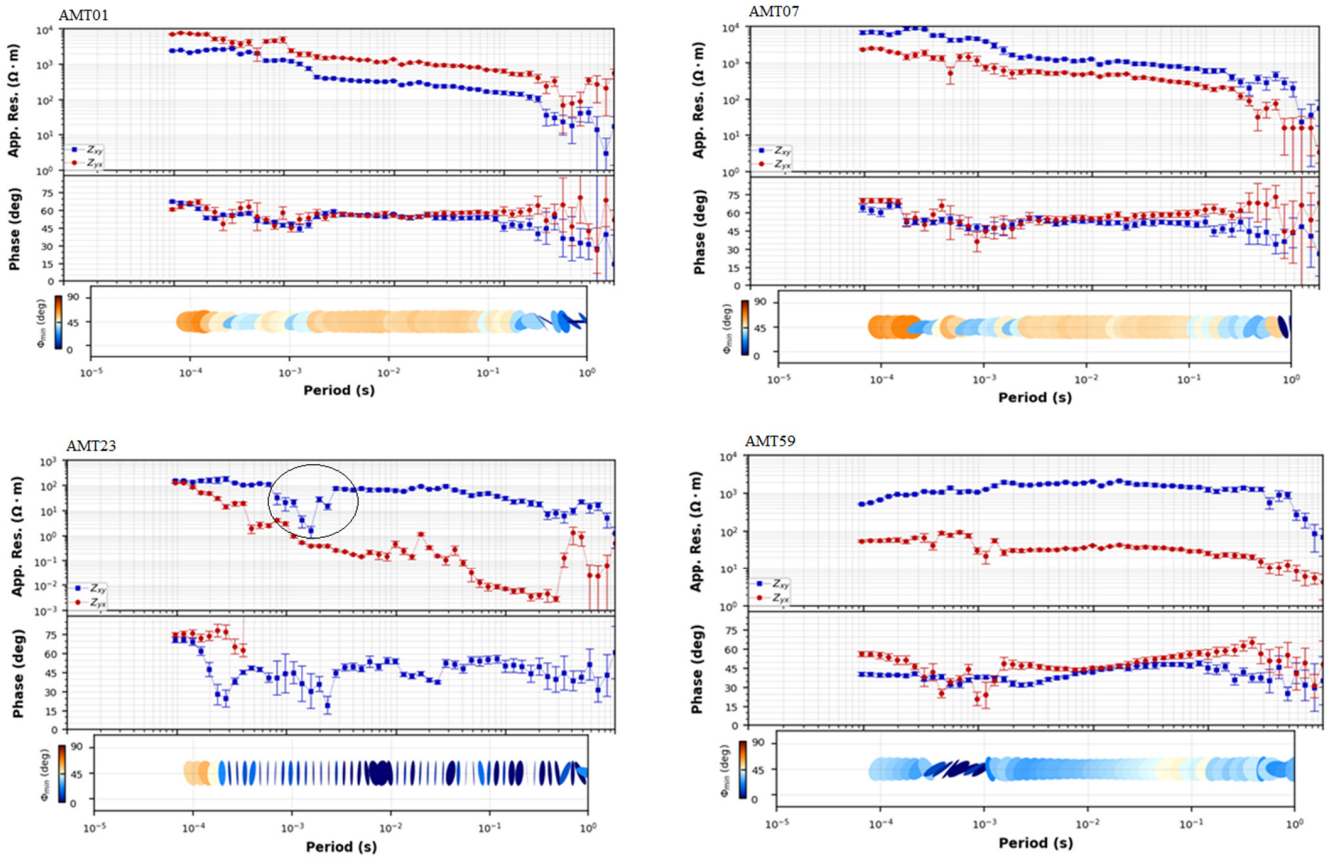

Figure 5. Observed apparent resistivity-phase curves and phase tensor ellipses for four representative AMT stations (AMT01, AMT07, AMT23 and AMT59). The black circle in AMT23 curve depicts interference in data.

6. Data Analysis

We performed data analysis and visualization of the processed AMT data for the properties of resistivity, phase, dimensionality, and geoelectric strike with the MTPy software package. The MTPy package is an open-source python library for magnetotelluric data analysis, developed by Geoscience Australia [64,65].

6.1. Apparent Resistivity-Phase Curves and Pseudo-Sections

Apparent resistivity and phase values for the off-diagonal components (Zxy and Zyx) of the impedance tensor and minimum phase tensor (Φmin) ellipses are shown in Figure 5 for the stations AMT01, AMT07, AMT23, and AMT59, located at different geological units. It is observed that apparent resistivity values are high, ranging from ~100–10,000 Ωm for stations AMT01 and AMT07, and ~10–2000 Ωm at ATM59. The resistivity range at AMT23 is comparatively low, with a maximum value of 100 Ωm. Stations AMT01 and AMT07 generally exhibit the same trends in the resistivity and phase curves. That is, high resistivity values are observed over a short period range, and low resistivities are observed for longer periods with phase angle above but asymptotic to 45°. The Φmin values show low to high characteristics, suggesting of response from both resistive and fairly conductive geological units. The curves for station AMT23 show noise due to interference in the acquired data. The noise is depicted by a sharp change of the curve at the period of 10^{-3} s in the Zxy component of the impedance tensor Z (Figure 5: AMT23 black circle). The corresponding Φmin is characterized by high values over short periods, which decrease with period increase. The underlying geological units at this station can be inferred to constitute both resistive and conductive lithologies. At Station AMT59, the apparent resistivity curve for Zxy increases while the phase curve drops for most periods (10^{-4} s–10^{-1} s). The Φmin

values are high at all periods. Thus, the geological formations at AMT59 can be interpreted as being highly electrically resistive.

Figure 6 shows the apparent resistivity pseudo-sections for the Zxx and Zyy components of Z for all stations. In both sections, at least two different structures can be speculated. These are highly conductive formations bound by electrically resistive formations on either side. The phase angle corresponding to the conductive formation is generally above 45° for Zxx data. A phase angle of <45° is evidently dominant for the Zyy data along the profile.

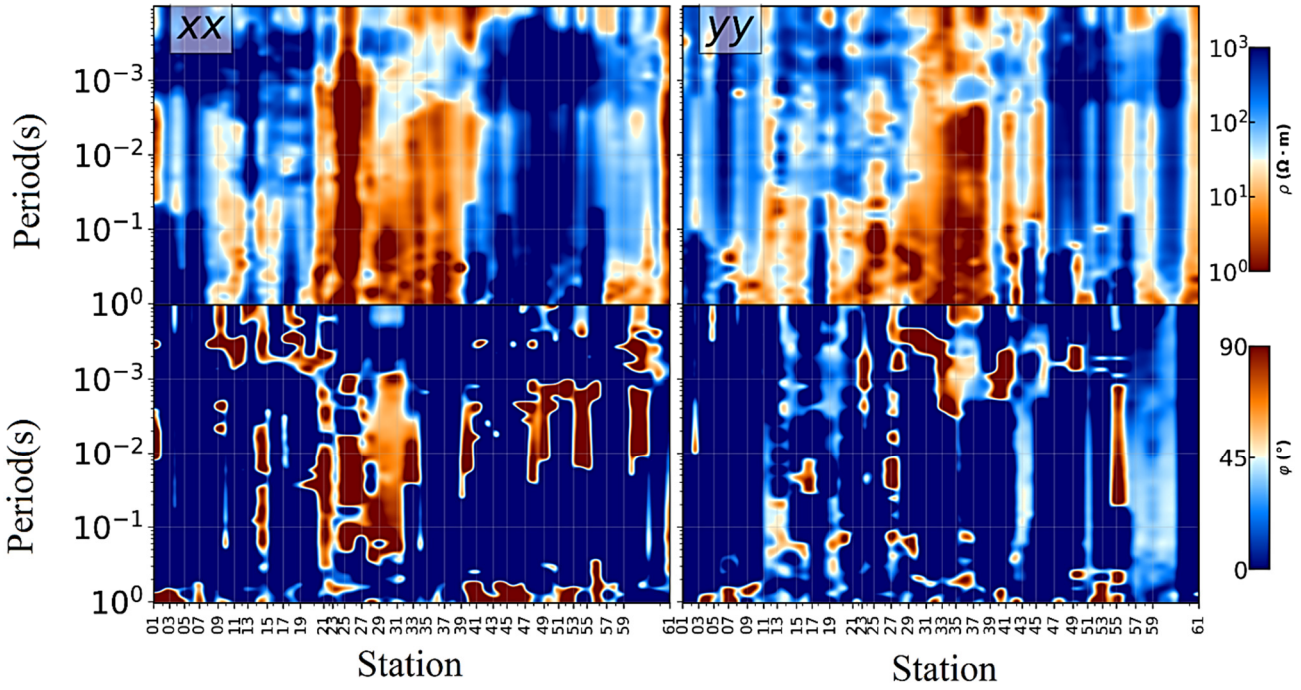

Figure 6. Apparent resistivity-phase pseudo-sections for Zxx and Zyy for an array of 61 stations across the Zhugongtang lead–zinc deposit. The upper panel shows resistivity and the lower panel represents phase, with Zxx as xx and Zyy as yy.

6.2. Dimensionality Analysis

We performed a dimensionality analysis of the AMT data prior to inversion to determine whether the computed impedance tensors, apparent resistivities, and phases at a specific frequency were related to one-, two-, or three-dimensional (1D, 2D or 3D) geoelectrical structures. Different researchers have proposed different dimensional tools to check the dimensionality of AMT data. In the present work, we analyzed dimensionality through the phase tensor method. Through the phase tensor method, no priori assumptions about the regional resistivity structure that we try to determine are made. In the phase tensor analysis, the relationship between the real and imaginary components of the impedance tensor of the observed data is described by the parameter skew (β) and is expressed as follows:

$$\beta = \frac{1}{2}\tan^{-1}\left(\frac{\phi_{xy} - \phi_{yx}}{\phi_{xx} + \phi_{yy}}\right) \quad (3)$$

The phase tensor skew (β) holds essential information about the dimensionality of the AMT data for the subsurface structure and its complexity [66]. For visual illustration, the phase tensor is graphically represented as an ellipse, and the value of the skew angle is represented by the color-coded ellipses as shown in Figure 7. For a 1D earth or a layered subsurface, the phase tensor is circular in shape, representing a small skew angle (β) [66]. In the case of a 2D regional resistivity structure, the phase tensor is elliptically shaped, with β becoming small. β is zero in data without errors [67]. For a 3D earth, the phase tensor is non-symmetric with β indicating large values. A rapid lateral change of the principal axes of the phase

tensor also indicates 3D structures [66]. In our study, a threshold of $|\beta| \leq \pm 5$ is considered for a 2D structure [22,68–70]. The analysis of the phase tensor pseudo-section plotted at different periods reveals the dimensionality of the subsurface structure (Figure 7). In the period interval 10^{-4} to 10^{-3} s, the phase tensor ellipses are dominated by a skew angle of $|\beta| \geq \pm 5°$, suggesting a 3D structure. However, the uppermost portion of the phase tensor pseudo section between AMT14–AMT20, AMT28–AMT39, and AMT52–AMT61 (except AMT56), the subsurface shows the skew angle of $|\beta| \leq \pm 5°$, suggesting a 2D structure. For the period interval of 10^{-3}–10^{-1} s, in the sections from AMT01–AMT11 and AMT27–AMT61, the skew angles are observed to have values $|\beta| \leq \pm 5°$. This range of β-values and the shape of the ellipses (Figure 7) imply the presence of 1D structure for values close to zero and 2D feature for values far from zero. During the same period, the subsurface between AMT12–AMT26 is suggested to have 1D, 2D, and 3D structures, as the β-values vary from 0 up to $\pm 8°$. For the period 10^{-1} to 1 s, all the AMT sites generally infer the existence of 2D and 3D structures. In summary, our AMT data have very large β-values and the phase tensors are elliptical and non-symmetric in shape. Therefore, we assume that the study area is characterized by 2D and 3D structures.

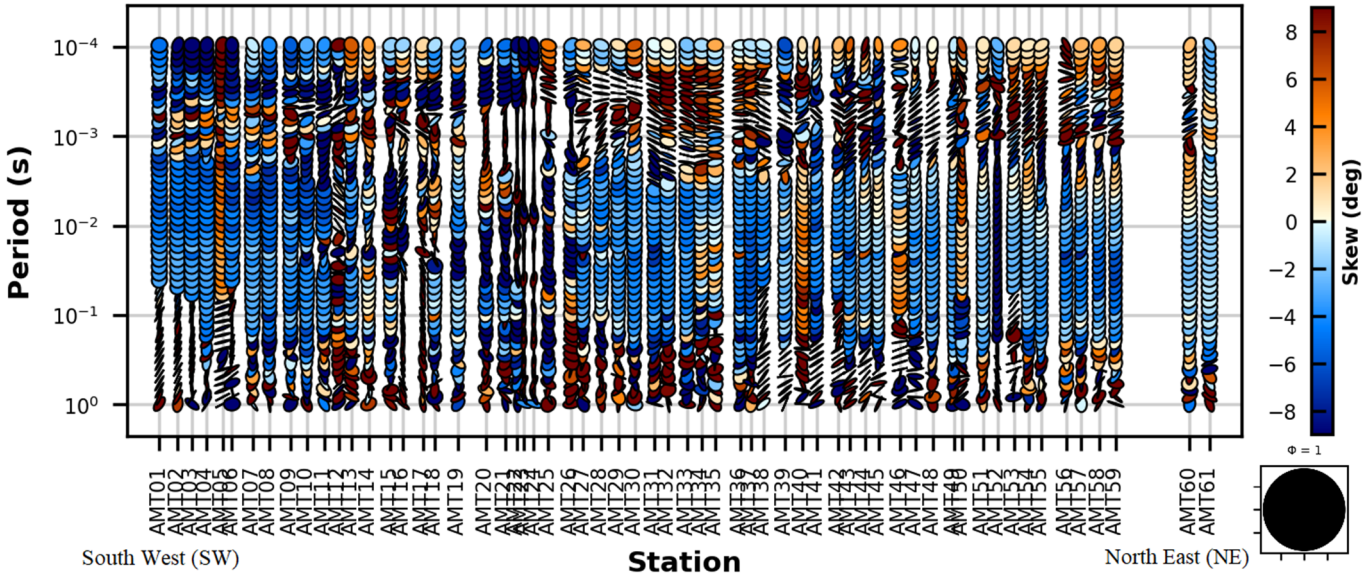

Figure 7. Phase tensor ellipses pseudo-section, color-coded by skew angle values along transect SW-NE. Four sites between AMT59 and AMT60 were neglected due the presence of cliffs.

6.3. Geoelectric Strike Estimation

The geoelectric strike is defined as the preferential direction representing the orientation of electric current flow in the subsurface [71]. The discussion from the previous subsection suggests that the study area has a 2D and 3D resistivity structure. Here, we have estimated the strike direction for the subsurface structures by the invariants of the impedance tensor (Z) and the phase tensor (PT) parameters. The obtained strikes are shown in Figure 8 as rose diagrams at different decades and all period ranges with the principal axis directions. A pair of dominant strikes were obtained by Z method observed to decrease from NE315° and NE40° at short period to NE285° and NE15° at long period respectively. A similar trend is exhibited for strikes obtained by PT approach which decrease from NE305° and NE35° to NE285°and NE17.5° respectively. At all periods, the Z pair of strikes converged to NE300° and NE27.5°, whereas the PT strikes converged to NE307° and NE35°. This strike analysis is inherently ambiguous by ±90°, implying that the geology of this area must also be taken into consideration. Simplified geological and cross-sectional maps of the study area (Figures 2 and 3) show that the Zhugongtang deposit is mainly controlled by several NW-trending (nearly parallel) faults, exhibiting similar strikes of roughly NE315°

as reported by other researchers [35,49,72]. Our results for the strike angle (at all periods) of NE300° and NE307° are in fairly good agreement with the NW–SE regional structure of the area. Therefore, in the AMT modelling, we used a strike direction of NE307° for the rotation of MT data. Strike angles of NE27.5 and NE35 were neglected, as they are not consistent with the structure in the study area.

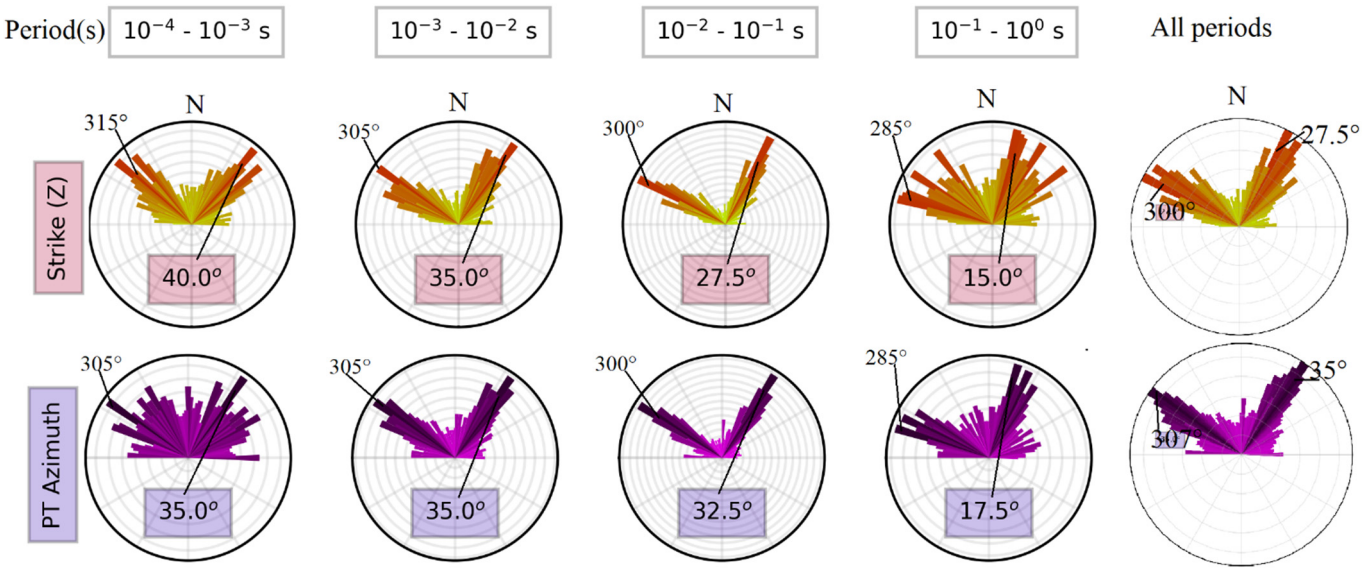

Figure 8. Multi-period rose diagrams of geoelectric strikes estimation at decade and at all periods from invariants of impedance tensor (Z) [73] and phase tensor (PT) [66]. North (N) is assumed to be 0 and the strike angle is measured clockwise positive.

7. Two-Dimensional Inversion

We inverted the rotated AMT data with the focused inversion algorithm contained in the ZONDMT2D software. This software package is designed for two-dimensional modelling and interpretation of MT data and was developed by Zond—a geophysical software developer in the Republic of Cyprus [74]. The focused inversion scheme uses the least square method with a smoothing operator and additional contrast focusing. As a result of this algorithm, piecewise smooth parameter distributions can be achieved. In other words, models which consist of blocks with constant resistivity can be obtained. Considering the high-elevation locations of 1.918–2.157 km (above sea level) of the study area, topographic relief was included in the 2D inverse modeling. This was done to reduce distortion in imaging based on acquired AMT data caused by rough topography. In the inversions, we considered transverse electric (TE), transverse magnetic (TM), and determinant or effective impedance (D) modes. The TE mode describes currents flowing parallel to strike, while the TM mode describes currents flowing perpendicular to strike. The determinant (effective impedance) mode describes the average of the impedance for all current directions. Prior to inverse modelling, we performed a static shift correction. This is because static shift is caused by near-surface inhomogeneities and noticeably complicate the interpretation of the apparent resistivity curves. This results in false geoelectric structures. The performed static shift correction was by done by identification and manually changing the curve level with reference to the adjacent curves using tools in ZONDMT2D. Additionally, an automatic static shift correction was also carried out on TE and TM data to suppress shifts by utilizing tools in the software (ZONDMT2D). We did not have access to TEM data that could be used to reliably correct the static shift. In the inversions process, we used 300 Ωm as an initial half-space value. For the inversion parameters, a smoothing factor of 1, depth smoothing of 1, smoothness ratio of 1, and focused threshold of 0.1 were set (more details on conditions of applying these factors can be found in [74]). Common model limits of 0.01 Ωm and 10,000 Ωm were assigned to the minimum and maximum resistivity, respectively. The

inversion was initially carried out for 30 iterations, then for 20 iterations, while adjusting the parameters for a better root mean square (RMS). The difference between modeled and measured datasets is captured in the RMS error and is usually presented as a percentage. RMS errors of less than 10% were considered acceptable in our 2D inverse modelling. After running the inversions, the final RMS error along the profile converged to 18.1% for TE, 9.7% for the TM mode and 9.1% for the D mode. The obtained models from the three inversion modes are further discussed in the next section.

8. Results and Discussion

The results of the 2D inversions in TE, TM, and D mode for AMT data collected across Zhugongtang deposit are shown in Figure 9, along with inversions error in RMS. The AMT models identify several regions of resistivity, which are also presented in Figure 10 and summarized in Table 1.

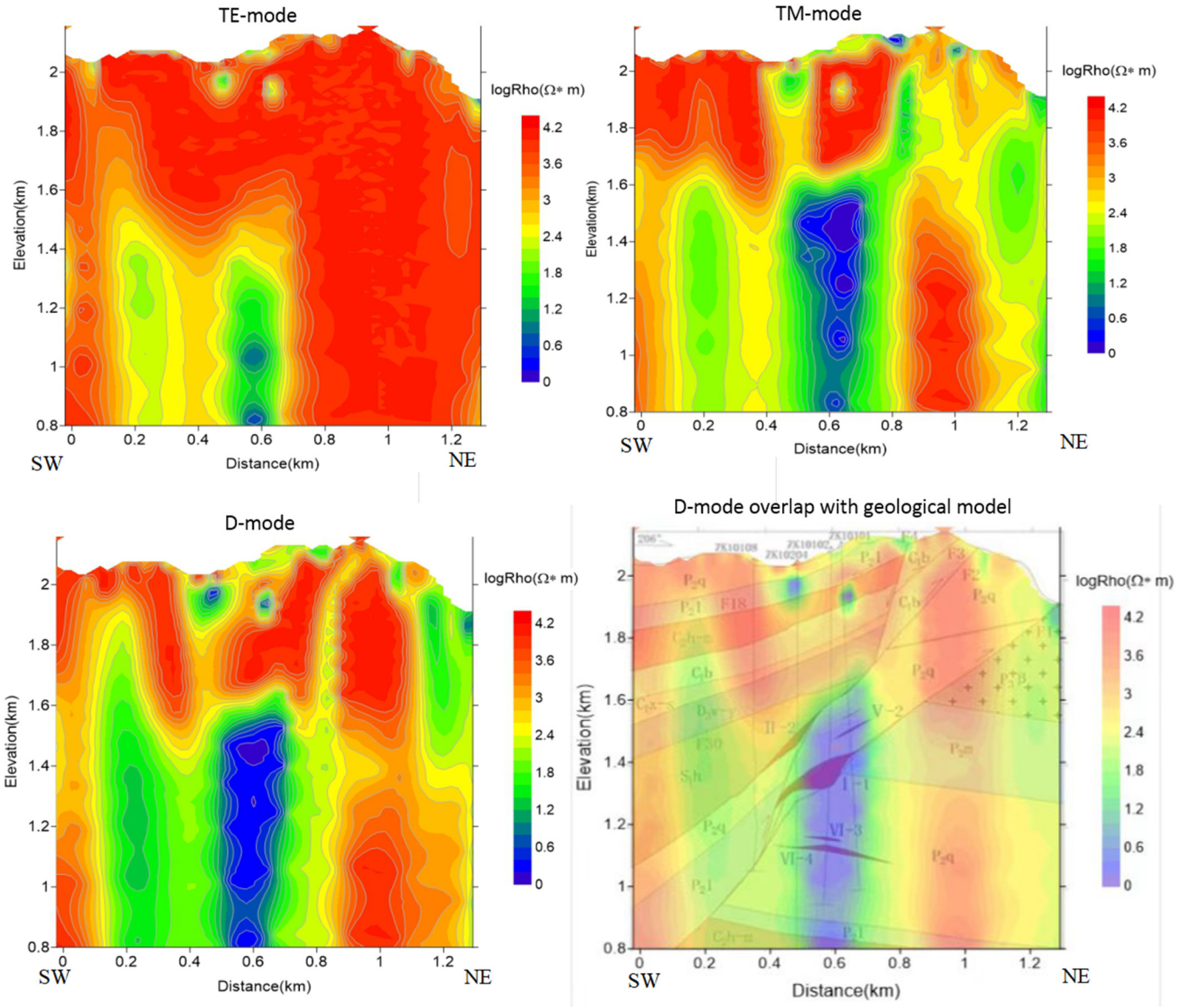

Figure 9. 2D inversion models of AMT data resolved by TE mode, TM mode, and D mode, obtained by ZondMT2D focused inversion and the overlap of the D- mode model with the geological model from Figure 3b. TE mode RMS = 18.1%. TM mode RMS = 9.7%. D-mode RMS = 9.1%.

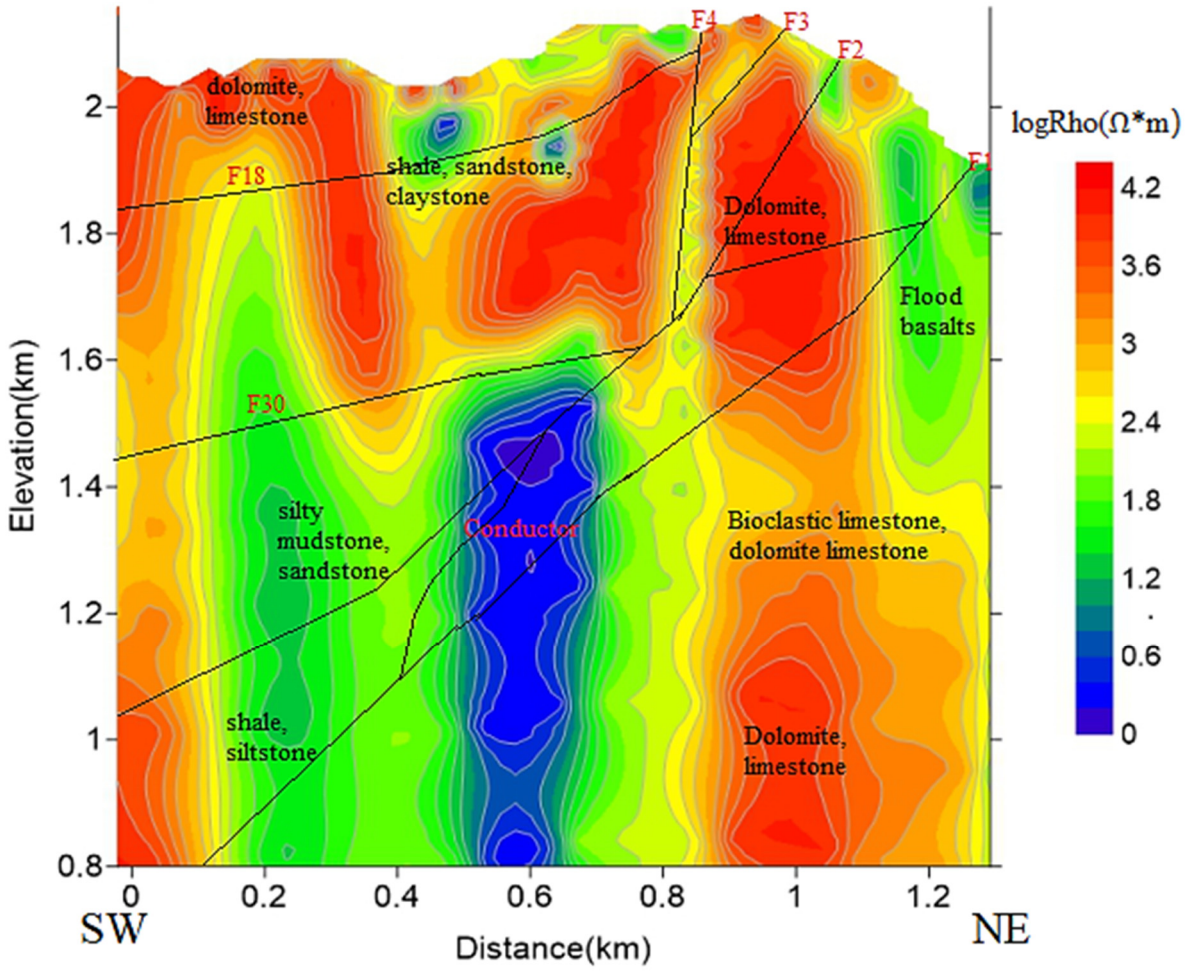

Figure 10. AMT resistivity cross-section across the Zhugongtang deposit showing inferred lithologic units and major faults.

Table 1. Rock and ore specimens resistivity comparison with AMT data in the study area.

Rock and Ore Specimens		Average Resistively/Ωm	Present Study: AMT Resistivity Range/Ωm
Dolomite and limestone		5551–157,130	≥1000
Basalts	tuffaceous basalt	517.3	>63 (flood basalts)
	massive basalt	2384	
Shale, sandstone, claystone Silty mudstone		<100	4–63
Bioclastic limestone, dolomite limestone			>250
Conductor (Pb-Zn)		69.4	<15

In the immediate SW section of the profile, the strata from the shallow to greater depths are observed to be highly resistive with variations between 250 Ωm and 10,000 Ωm. The three modes resolved a resistive section bound by an offset distance of 0–0.15 km, which were inferred to be dolomite and limestone dominated zones. A conductive zone (<63 Ωm) is evident in the subsurface and defined by offset distances of 0.15–0.30 km at approximately 400 m depth and extend deeper and are overlaid by inferred resistive dolomite and limestone units. We interpret that this conductive zone is due to silty mudstone, sandstone, shale, claystone, and siltstones, belonging to the Silurian Hanjiangdian(S_1h) and

Permian Longtan(P_2l) Fm. The enhanced conductivity of this zone may be attributed to faults (Figure 10) and probable disseminated conductive minerals.

The central section of the profile has two distinct anomalous features, which are several small units of low resistivity features (<63 Ωm) imbedded in superficial depths and a significantly low electrical resistivity conductor (<15 Ωm) at a greater depth. The small units of low resistivity are confined by 0.30–1.28 km of distance and rest at a maximum depth of 0.10 km (above 1.9 km of elevation). The small units are thought to be associated with mudstones on the basis of their resistivity signatures and in reference to the geology of the area. The significantly low electrical resistivity of the conductor (<15 Ωm) is restricted by 0.3–0.8 km of horizontal distance and is evident from the minimum depth of 0.5 km, which extends into deeper strata. We deduce that this deep-seated low resistivity anomaly is due to mineralization of lead- and zinc-based metals. This is supported by a good overlap between obtained resistivity models and geological model for the location of the best conductor in the study area.

The subsurface materials in the NE section of the profile exhibit high resistivity values, ranging from shallow to greater depth, in the TE model. This is contrary to the results obtained by TM and D modes. The TM and D modes reveal moderate to high resistivity material in the shallow subsurface, and high resistivity material in the deep subsurface. The NE subsurface consists of four major faults: F1, F2, F3, and F4 (Figures 2 and 10), which are likely to exhibit low resistivity. According to Unsworth (1999), faults can increase permeability parallel to the faults line and inhibit the movement of materials perpendicular to the faults. In addition, faults can trap fluids in gouge- and fault- breccia [75]. Consequently, changing the electrical resistivity of the subsurface and influencing the preferred current flow direction [75]. In this work, the faults and their conductivity enhancing effects are not evident in the TE model, but rather evident in the TM and D mode. This demonstrates that TE and TM geoelectric models support the concept of information complementarity [76]. That is, structures missed by TE mode are defined in the TM mode, and those omitted by TM revealed in TE mode. We also observe that the TE mode is most responsive to conductors along the strike and the TM mode is better at identifying resistivity interfaces such as across faults and boundaries, owing to interface charge build-up [77]. In the TM geoelectric model, the NE upper area, with several faults bound between 0.8 and 1.28 km of distance and between 1.6 and 2 km of elevation are estimated to have resistivity that varies between 100–500 Ωm. This is more likely attributed to faults in dolomite and limestone units. Again, in the same distance (0.8–1.28 km) at elevations between 1.2 and 1.4 km, another moderate–high resistivity anomaly (>250 Ωm) is encountered. Through interpretation, it is associated with bioclastic limestone and dolomite limestone from the Permian Maokou Fm (P_2m). The subsurface outlined by a distance between 1.1 and 1.28 km, at an elevation between 1.4 and 1.9 km shows a low–moderate resistivity zone (>63 Ωm) revealed in TM and D mode. This is inferred to be basalt rock of the upper Permian Emeishan ($P_3\beta$) strata.

9. Conclusions

In this study, the geoelectrical signature across the known location of lead–zinc mineralization in the Zhugongtang orefield was investigated by applying the AMT procedure to a single survey line. The results confirm the presence of conducting bodies: (a) small and large sized zones (<63 Ωm) in surficial depth (<0.10 km), and claystone, silty mudstone, shale and sandstone, to be more likely at deeper depths (>0.10 km), and (b) large sized conductors (<15 Ωm) at greater depths (≥0.50 km), which are inferred to be Pb–Zn mineralization. The geoelectrical strike estimated using the phase tensor and impedance tensor methods show satisfactory results and are in a good agreement with the structure of the Zhugongtang mining area for the NW–SE direction. Two-dimensional resistivity models obtained for the study area could not clearly distinguish the boundaries between lithologic layers. However, the wide distribution of dolomite and limestone is evident in models and mineral-bearing geological formations are coincident with the low resistivity region. Furthermore, formation of flood basalts are also imaged in the study area. Moreover, rock

and ore specimen data show fairly good agreement with AMT resistivity data. Likewise, regions with a high fault density were found to be fairly conductive compared to regions with low fault density. All in all, the 2D inversion with topography of AMT data can visually show the distribution of major structures across the lead–zinc deposit in a region with strong EM interferences and high elevations. Hence, these findings are a contribution to the current literature on Zhugongtang deposit and may be useful for future research work in the same or similar areas.

Author Contributions: R.P., M.L., R.C., G.N., S.C., H.Y., R.S. and E.J. contributed equally in the writing of this paper. All authors have read and approved the final manuscript. All authors have read and agreed to the published version of the manuscript.

Funding: This research was funded by Basic Science Center Project of National Natural Science Foundation of China, grant number 72088101.

Data Availability Statement: The EDI files and coordinate information of all AMT sites can be obtained on request by contacting the corresponding author.

Acknowledgments: We would like to thank the anonymous reviewers and academic editors for taking the time and effort to review the manuscript. We appreciate all valuable comments and suggestions, which improved the quality of the manuscript.

Conflicts of Interest: The authors declare no conflict of interest.

References

1. Andrieu, B.; Vidal, O.; le Boulzec, H.; Verzier, F. Modelling the Demand and Access of Mineral Resources in a Changing World. *Sustainability* **2022**, *14*, 11.
2. Nkuna, R.; Ijoma, G.; Matambo, T.; Chimwani, N. Accessing Metals from Low-Grade Ores and the Environmental Impact Considerations: A Review of the Perspectives of Conventional versus Bioleaching Strategies. *Minerals* **2022**, *12*, 506. [CrossRef]
3. Zhdanov, M.S. Editorial for Special Issue Geophysics for Mineral Exploration. *Minerals* **2021**, *11*, 692. [CrossRef]
4. Zhang, G.; Lü, Q.T.; Zhang, G.B.; Lin, P.R.; Jia, Z.Y.; Suo, K. Joint interpretation of geological, magnetic, AMT, and ERT data for mineral exploration in the Northeast of Inner Mongolia, China. *Pure Appl. Geophys.* **2018**, *175*, 989–1002. [CrossRef]
5. Zhao, P.; Cheng, Q.; Xia, Q. Quantitative Prediction for Deep Mineral Exploration. *J. China Univ. Geosci.* **2008**, *19*, 309–318.
6. Fu, J.; Jia, S.; Wang, E. Combined Magnetic, Transient Electromagnetic, and Magnetotelluric Methods to Detect a BIF-Type Concealed Iron Ore Body: A Case Study in Gongchangling Iron Ore Concentration Area, Southern Liaoning Province, China. *Minerals* **2020**, *10*, 1044. [CrossRef]
7. Embeng, S.B.N.; Meying, A.; Ndougsa-Mbarga, T.; Moreira, C.A.; Amougou, O.U.O. Delineation and Quasi-3D Modeling of Gold Mineralization Using Self-Potential (SP), Electrical Resistivity Tomography (ERT), and Induced Polarization (IP) Methods in Yassa Village, Adamawa, Cameroon: A Case Study. *Pure Appl. Geophys.* **2022**, *179*, 795–815. [CrossRef]
8. Zhang, J.; Zeng, Z.; Zhao, X.; Li, J.; Zhou, Y.; Gong, M. Deep Mineral Exploration of the Jinchuan Cu–Ni Sulfide Deposit Based on Aeromagnetic, Gravity, and CSAMT Methods. *Minerals* **2020**, *10*, 168. [CrossRef]
9. Jiang, W.; Duan, J.; Michael, D.; Clark, A.; Schofield, A.; Brodie, R.C.; Goodwin, J. Application of multiscale magnetotelluric data to mineral exploration: An example from the east Tennant region, Northern Australia. *Geophys. J. Int.* **2022**, *229*, 1628–1645. [CrossRef]
10. Gan, J.; Li, H.; He, Z.; Gan, Y.; Mu, J.; Liu, H.; Wang, L. Application and Significance of Geological, Geochemical, and Geophysical Methods in the Nanpo Gold Field in Laos. *Minerals* **2022**, *12*, 96. [CrossRef]
11. Lap, T.T. Application of Audio-Magnetotelluric Method for Exploration the Concealed Ore-Bodies in Yuele Lead-Zinc Ore Feild, Daguan County, NE Yunnan Province, China. *J. Geosci. Environ. Prot.* **2014**, *2*, 35–45. [CrossRef]
12. Lap, T.T.; Xue, C.; Qureshijavedakhter; Wei, A.; Liu, L.; Li, W. Audio-Magnetotelluric Surveying and Its Application For The Concealed Orebodies Prospecting In Yuele Lead-Zinc Deposit Area, Daguan District, Northeastern Yunnan Province, China. *Int. J. Appl. Nat. Sci.* **2014**, *3*, 5–14.
13. Chen, R.; He, M.; Chang, F.; Zeng, P.; Zhao, X. Large-scale 3-D inversion of AMT data with application to mineral exploration. In Proceedings of the 23rd Electromagnetic Induction Workshop—EMIW2016, Chiang Mai, Thailand, 14–21 August 2016.
14. Bagchi, A.; Shalivahan, R.K.S.; Sinharay, R.K. 3D Phase tensor inversion and Joint inversion using impedance and phase tensor components aiming better subsurface mapping and interpretation in Dhanjori basin, Singhbhum craton, eastern India. *J. Appl. Geophys.* **2022**, *202*, 104646. [CrossRef]
15. Bastani, M.; Malehmir, A.; Ismail, N.; Pedersen, L.B.; Hedjazi, F. Delineating hydrothermal stockwork copper deposits using controlled-source and radio-magnetotelluric methods: A case study from northeast Iran. *Geophysics* **2009**, *74*, B167–B181. [CrossRef]

16. Agyemang, V.O. Groundwater exploration by magnetotelluric method within the birimian rocks of mankessim, Ghana. *Appl. Water Sci.* **2022**, *12*, 26. [CrossRef]
17. Carlson, N.R.; Paski, P.M.; Urquhart, S.A. Applications of Controlled Source and Natural Source Audio-Frequency Magnetotellurics to Groundwater Exploration. In Proceedings of the 18th EEGS Symposium on the Application of Geophysics to Engineering and Environmental Problems, Atlanta, GA, USA, 3–7 April 2005.
18. Zaher, M.A.; Younis, A.; Shaaban, H.; Mohamaden, M.I. Integration of geophysical methods for groundwater exploration: A case study of El Sheikh Marzouq area, Farafra Oasis, Egypt. *Egypt. J. Aquat. Res.* **2021**, *47*, 239–244. [CrossRef]
19. He, G.L.; Wang, G.J.; Zhou, C.; Yan, X.L.; Li, H.L. Application of Audio-frequency Magnetotelluric (AMT) in groundwater exploration: A case of the Nanmushui area in Zhanjiang. *Prog. Geophys.* **2019**, *34*, 304–309.
20. Ishizu, K.; Ogawa, Y.; Mogi, T.; Yamaya, Y.; Uchida, T. Ability of the magnetotelluric method to image a deep conductor: Exploration of a supercritical geothermal system. *Geothermics* **2021**, *96*, 102205. [CrossRef]
21. He, L.; Chen, L.; Xi, X.; Zhao, X.; Chen, R.; Yao, H. Mapping the Geothermal System Using AMT and MT in the Mapamyum (QP) Field, Lake Manasarovar, Southwestern Tibet. *Energies* **2016**, *9*, 855. [CrossRef]
22. Deshmukh, V.; Kumar, P.V.; Rao, P.S.; Kumar, A.; Singh, A. Audiomagnetotelluric (AMT) studies across Aravali-Tural-Rajawadi geothermal zones, western Maharastra, India. *J. Appl. Geophys.* **2022**, *198*, 104579. [CrossRef]
23. Sandberg, S.K.; Hohmann, G.W. Controlled-source audiomagnetotellurics in geothermal exploration. *Geophysics* **1982**, *47*, 100–116. [CrossRef]
24. Wu, G.; Hu, X.; Huo, G.; Zhou, X. Geophysical exploration for geothermal resources: An application of MT and CSAMT in Jiangxia, Wuhan, China. *J. Earth Sci.* **2012**, *23*, 757–767. [CrossRef]
25. Min, G.; Wang, X.; Zhang, J.; Liu, K.; Yuan, H. The Concept of Multi-scale MT Interpretation Strategy and Its Application in Guizhou Province of China. *Pure Appl. Geophys.* **2022**, *179*, 1037–1051. [CrossRef]
26. Robertson, K.; Taylor, D.; Thiel, S.; Heinson, G. Magnetotelluric evidence for serpentinisation in a Cambrian subduction zone beneath the Delamerian Orogen, southeast Australia. *Gondwana Res.* **2015**, *28*, 601–611. [CrossRef]
27. Share, P.E.; Jones, A.G.; Muller, M.R.; Khoza, D.T.; Miensopust, M.P.; Webb, S.J. An audio-magnetotelluric investigation of the Otjiwarongo and Katima Mulilo regions, Namibia. *Geophysics* **2014**, *79*, B151–B171. [CrossRef]
28. Bastani, M.; Wang, S.; Malehmir, A.; Mehta, S. Radio-magnetotelluric and controlled-source magnetotelluric surveys on a frozen lake: Opportunities for urban applications in Nordic countries. *Near Surf. Geophys.* **2022**, *20*, 30–45. [CrossRef]
29. Mehta, S. Radio Magnetotelluric (RMT) measurement over lake Mälaren, Sweden: A case study. *Geol. Geophys. Environ.* **2015**, *41*, 110. [CrossRef]
30. Mehta, S.; Bastani, M.; Malehmir, A.; Pedersen, L.B. Resolution and sensitivity of boat-towed RMT data to delineate fracture zones–example of the Stockholm bypass multi-lane tunnel. *J. Appl. Geophys.* **2017**, *139*, 131–143. [CrossRef]
31. Saraev, A.; Antashuk, K.; Simakov, A.; Shlykov, A.; Konkov, A. Near surface exploration for horizontal welling using CSRMT method: Case study. In Proceedings of the International Conference on Engineering Geophysics, Al Ain, United Arab Emirates, 9–12 October 2017.
32. Tezkan, B.; Hördt, A.; Gobashy, M. Two-dimensional radiomagnetotelluric investigation of industrial and domestic waste sites in Germany. *J. Appl. Geophys.* **2000**, *44*, 237–256. [CrossRef]
33. Wang, S.; Malehmir, A.; Bastani, M. Geophysical characterization of areas prone to quick-clay landslides using radio-magnetotelluric and seismic methods. *Tectonophysics* **2016**, *677–678*, 248–260. [CrossRef]
34. Luo, K.; Zhou, J.X.; Sun, G.T.; Nguyen, A.; Qin, Z.X. The metallogeny of the Devonian sediment-hosted sulfide deposits, South China: A case study of the Huodehong deposit. *Ore Geol. Rev.* **2022**, *143*, 104747. [CrossRef]
35. Wei, C.; Huang, Z.; Ye, L.; Hu, Y.; Santosh, M.; Wu, T.; He, L.; Zhang, J.; He, Z.; Xiang, Z.; et al. Genesis of carbonate-hosted Zn-Pb deposits in the Late Indosinian thrust and fold systems: An example of the newly discovered giant Zhugongtang deposit, South China. *J. Asian Earth Sci.* **2021**, *220*, 104914. [CrossRef]
36. Metcalfe, I. Palaeozoic and Mesozoic tectonic evolution and palaeogeography of East Asian crustal fragments: The Korean Peninsula in context. *Gondwana Res.* **2006**, *9*, 24–46. [CrossRef]
37. Charvet, J.; Shu, L.; Shi, Y.; Guo, L.; Faure, M. The building of south China: Collision of Yangzi and Cathaysia blocks, problems and tentative answers. *J. Southeast Asian Earth Sci.* **1996**, *13*, 223–235. [CrossRef]
38. Zhang, W.D.; You, H.T.; Li, B.; Zhao, K.D.; Chen, X.D.; Zhu, L. Ore-forming processes of the Qixiashan carbonate-hosted Pb-Zn deposit, South China: Constraints from sulfide trace elements and sulfur isotopes. *Ore Geol. Rev.* **2022**, *143*, 104786. [CrossRef]
39. Zhang, C.; Wu, Y.; Hou, L.; Mao, J. Geodynamic setting of mineralization of Mississippi Valley-type deposits in world-class Sichuan–Yunnan–Guizhou Zn–Pb triangle, southwest China: Implications from age-dating studies in the past decade and the Sm–Nd age of Jinshachang deposit. *J. Asian Earth Sci.* **2015**, *103*, 103–114. [CrossRef]
40. Yang, Q.; Liu, W.; Zhang, J.; Wang, J.; Zhang, X. Formation of Pb–Zn deposits in the Sichuan–Yunnan–Guizhou triangle linked to the Youjiang foreland basin: Evidence from Rb–Sr age and in situ sulfur isotope analysis of the Maoping Pb–Zn deposit in northeastern Yunnan Province, southeast China. *Ore Geol. Rev.* **2019**, *107*, 780–800. [CrossRef]
41. Oyebamiji, A.; Hu, R.; Zhao, C.; Zafar, T. Origin of the Triassic Qilinchang Pb-Zn deposit in the western Yangtze block, SW China: Insights from in-situ trace elemental compositions of base metal sulphides. *J. Asian Earth Sci.* **2020**, *192*, 104292. [CrossRef]
42. Wu, Y.; Zhang, C.; Mao, J.; Ouyang, H.; Sun, J. The genetic relationship between hydrocarbon systems and Mississippi Valley-type Zn–Pb deposits along the SW margin of Sichuan Basin, China. *Int. Geol. Rev.* **2013**, *55*, 941–957. [CrossRef]

43. Zhao, D.; Han, R.; Wang, L.; Ren, T.; Wang, J.; Zhang, X.; Cui, J.; Ding, J. Genesis of the Lehong large zinc–lead deposit in northeastern Yunnan, China: Evidences from geological characteristics and C–H–O–S–Pb isotopic compositions. *Ore Geol. Rev.* **2021**, *135*, 104219. [CrossRef]
44. Shen, X.; Lin, H.; Zhang, B.; Du, Q. The genesis of Guanting Pb–Zn deposits in the Jianshui area, Yunnan Province, SW China: Constraints from geochronology, S isotopes and trace elements. *Mineral. Petrol.* **2022**, *116*, 47–69. [CrossRef]
45. Li, Z.X.; Li, X.H.; Wartho, J.A.; Clark, C.; Li, W.X.; Zhang, C.L.; Bao, C. Magmatic and metamorphic events during the early Paleozoic Wuyi Yunkai orogeny, southeastern South China: New age constraints and pressure-temperature conditions. *GSA Bull.* **2010**, *122*, 772–793. [CrossRef]
46. Carter, A.; Clift, P.D. Was the Indosinian orogeny a Triassic mountain building or a thermotectonic reactivation event? *Comptes Rendus Geosci.* **2008**, *340*, 83–93. [CrossRef]
47. Shellnutt, J.G.; Vaughan, M.W.; Lee, H.Y.; Iizuka, Y. Late Jurassic Leucogranites of Macau (SE China): A Record of Crustal Recycling During the Early Yanshanian Orogeny. *Front. Earth Sci.* **2020**, *8*, 311. [CrossRef]
48. Zhou, J.X.; Xiang, Z.Z.; Zhou, M.F.; Feng, Y.X.; Luo, K.; Huang, Z.L.; Wu, T. The giant Upper Yangtze Pb–Zn province in SW China: Reviews, new advances and a new genetic model. *J. Asian Earth Sci.* **2018**, *154*, 280–315. [CrossRef]
49. He, L.; Wu, D.; Zhao, F.; Jin, X.; Bai, G.; Chen, Z.; Wang, J.; Huang, Q.; Cai, J. Geological Characteristics, Exploration Model and Prospecting Direction of the Zhugongtang Ultra—large Pb—Zn deposit in Guizhou Province. *Guizhou Geol.* **2019**, *36*, 101–109. (In Chinese with English Abstract).
50. Tikhonov, A.N. On determining electrical characteristics of the deep layers of the Earth's crust. *Doklady* **1950**, *73*, 281–285.
51. Cagniard, L. Basic theory of the magneto-telluric method of geophysical prospecting. *Geophysics* **1953**, *18*, 605–635. [CrossRef]
52. Cantwell, T. Detection and Analysis of Low Frequency Magnetotelluric Signals. Doctoral Dissertation, Massachusetts Institute of Technology, Cambridge, MA, USA, 1960.
53. Cantwell, T.; Madden, T.R. Preliminary report on crustal magnetotelluric measurements. *J. Geophys. Res.* **1960**, *65*, 4202–4205. [CrossRef]
54. Vozoff, K. The magnetotelluric method in the exploration of sedimentary basins. *Geophysics* **1972**, *37*, 98–141. [CrossRef]
55. Singh, R.K.; Shalivahan, V.P.M.; Singh, S. Imaging Regional Geology and Au—Sulphide mineralization over Dhanjori greenstone belt: Implications from 3-D Inversion of Audio Magnetotelluric data and Petrophysical Characterization. *Ore Geol. Rev.* **2019**, *106*, 369–386. [CrossRef]
56. Tezkan, B. Radiomagnetotellurics. In *Groundwater Geophysics*; Springer: Berlin/Heidelberg, Germany, 2009.
57. Kalscheuer, T.; Juhojuntti, N.; Vaittinen, K. Two-Dimensional Magnetotelluric Modelling of Ore Deposits: Improvements in Model Constraints by Inclusion of Borehole Measurements. *Surv. Geophys.* **2018**, *39*, 467–507. [CrossRef]
58. Chave, A.D.; Jones, A.G. *The Magnetotelluric Method: Theory and Practice*; Cambridge University Press: New York, NY, USA, 2012.
59. Nabighian, M.N. *Electromagnetic Methods in Apllied Geophysics 2*; Nabighian, M.N., Ed.; Society of Exploration Geophysicists: Houston, TX, USA, 1991; pp. 641–712.
60. Lindsay, M.D.; Spratt, J.; Occhipinti, S.A.; Aitken, A.R.; Dentith, M.C.; Hollis, J.A.; Tyler, I.M. Identifying mineral prospectivity using 3D magnetotelluric, potential field and geological data in the east Kimberley, Australia. *Geol. Soc. Lond. Spec. Publ.* **2017**, *453*, 247–268. [CrossRef]
61. Li, F.; Zeng, Q.; Zhu, R.; Chu, S.; Xie, W.; Zhang, B.; Zhang, X. Application of the AMT Method to Gold Deposits: A Case Study in the Qinling Metallogenic Belt of North China Craton. *Minerals* **2021**, *11*, 1200. [CrossRef]
62. GSAI Geophysics. Internet of Things Broadband Magnetotelluric Instrument GSEM-W10. GSAI Geophysics, [Online]. Available online: http://www.gs-ait.com/productinfo/432117.html (accessed on 10 October 2022).
63. GSAI Geophysics. Electromagnetic Data Processing Software GSEM-Pros. GSAI Geophysics, [Online]. Available online: http://www.gs-ait.com/productinfo/432127.html (accessed on 10 October 2022).
64. Kirkby, A.L.; Zhang, F.; Peacock, J.; Hassan, R.; Duan, J. The MTPy software package for magnetotelluric data analysis and visualisation. *J. Open Source Softw.* **2019**, *4*, 1358. [CrossRef]
65. Krieger, L.; Peacock, J. MTpy: A Python toolbox for magnetotellurics. *Comput. Geosci.* **2014**, *72*, 167–175. [CrossRef]
66. Caldwell, T.G.; Bibby, H.M.; Brown, C. The magnetotelluric phase tensor. *Geophys. J. Int.* **2004**, *158*, 457–469. [CrossRef]
67. Booker, J.R. The magnetotelluric phase tensor: A critical review. *Surv. Geophys.* **2014**, *35*, 7–40. [CrossRef]
68. Thiel, S.; Heinson, G.; Gray, D.R.; Gregory, R.T. Ophiolite emplacement in NE Oman: Constraints from magnetotelluric sounding. *Geophys. J. Int.* **2009**, *176*, 753–766. [CrossRef]
69. Farzamian, M.; Ribeiro, J.A.; Khalil, M.A.; Santos, F.A.M.; Kashkouli, M.F.; Bortolozo, C.; Mendonça, J.L. Application of transient electromagnetic and audio-magnetotelluric methods for imaging the Monte real aquifer in Portugal. *Pure Appl. Geophys.* **2019**, *176*, 719–735. [CrossRef]
70. Seki, K.; Kanda, W.; Ogawa, Y.; Tanbo, T.; Kobayashi, T.; Hino, Y.; Hase, H. Imaging the hydrothermal system beneath the Jigokudani valley, Tateyama volcano, Japan: Implications for structures controlling repeated phreatic eruptions from an audio-frequency magnetotelluric survey. *Earth Planets Space* **2015**, *67*, 6. [CrossRef]
71. Niasari, S.W. A short introduction to geological strike and geo-electrical strike. *AIP Conf. Proc.* **2016**, *1755*, 100002.
72. Wu, D.; He, L.; Cai, J.; Wang, J.; Bai, G.; Yang, T.; Jin, X.; Huang, Q. Main Orebody Characteristics and Ore—prospecting Symbols of Zhugongtang Lead—zinc Deposit in Hezhang, Guizhou. *Guizhou Geol.* **2019**, *36*, 299–306 (In Chinese with English Abstract).

73. Weaver, J.T.; Agarwal, A.K.; Lilley, F.E.M. Characterization of the magnetotelluric tensor in terms of its invariants. *Geophys. J. Int.* **2000**, *141*, 321–336. [CrossRef]
74. ZOND Geophysical Software, ZondMT2D. ZOND Geophysical Software, 2001–2022. Available online: http://zond-geo.com/english/zond-software/electromagnetic-sounding/zondmt2d/ (accessed on 20 March 2022).
75. Unsworth, M.; Egbert, G.; Booker, J. High-resolution electromagnetic imaging of the San Andreas fault in Central California. *J. Geophys. Res.* **1999**, *104*, 1131–1150. [CrossRef]
76. Maulinadya, S.; Grandis, H. Geoelectric Strike Analysis from Magnetotelluric (MT) Data Using Swift and Polar Diagram Methods. *IOP Conf. Ser. Earth Environ. Sci.* **2019**, *318*, 012049. [CrossRef]
77. Berdichevsky, M.N.; Dmitriev, V.I.; Pozdnjakova, E.E. On two-dimensional interpretation of magnetotelluric soundings. *Geophys. J. Int.* **1998**, *133*, 585–606. [CrossRef]